

Atomic Regional Superfluids in two-dimensional Moiré Time Crystals

Weijie Liang,¹ Weiping Zhang,^{2,3,4,5,*} and Keye Zhang^{1,3,†}

¹Quantum Institute for Light and Atoms, State Key Laboratory of Precision Spectroscopy, Department of Physics, School of Physics and Electronic Science, East China Normal University, Shanghai 200062, China

²School of Physics and Astronomy, and Tsung-Dao Lee Institute, Shanghai Jiao Tong University, Shanghai 200240, China

³Shanghai Branch, Hefei National Laboratory, Shanghai 201315, China

⁴Shanghai Research Center for Quantum Sciences, Shanghai 201315, China

⁵Collaborative Innovation Center of Extreme Optics, Shanxi University, Taiyuan, Shanxi 030006, China

Moiré physics has transcended spatial dimensions, extending into synthetic domains and enabling novel quantum phenomena. We propose a theoretical model for a two-dimensional (2D) Moiré time crystal formed by ultracold atoms, induced by periodic perturbations applied to a non-lattice trap. Our analysis reveals the emergence of regional superfluid states exhibiting moiré-scale quantum coherence across temporal, spatial, and spatiotemporal domains. This work provides fundamental insights into temporal moiré phenomena and presents an alternative pathway to engineer spatial moiré phases without requiring twisted multilayer lattices.

Introduction.—Twistronics has revolutionized quantum materials science through interlayer rotation in 2D systems, enabling discoveries from unconventional superconductivity in twisted bilayer graphene [1–6] to topologically protected quantum devices [7–10] and novel quantum phases in Moiré lattices [11–17]. While its quantum simulations using atomic Bose-Einstein condensates (BECs) in Moiré optical lattices [18] and photonic Moiré crystals [19–22] have surpassed solid-state parameter control limits, these approaches remain constrained by two fundamental requirements, physical twisted lattice structures and exclusive focus on spatial dimensions. Recent demonstrations of frequency-domain Moiré lattices [23] suggest twistronics’ potential in synthetic dimensions. However, the temporal Moiré lattices and the intrinsic link between spatial and temporal Moiré physics in quantum many-body systems remain unexplored. Specifically, temporal Moiré phases are expected to offer advantages to quantum applications, analogous to those provided by their spatial counterparts but operating in the time domain [24–29].

We present a lattice-free scheme for unified spatial and temporal twistronics simulations using a moving BEC within a deeply confined 2D potential well subjected to multi-frequency “bobbing” modulation. This approach eliminates the requirement for complex multilayer lattice potentials [18, 30] or engineered interlayer tunneling [31], while generating both spatial and temporal Moiré quantum phases. These phases exhibit characteristic regional superfluidity with Moiré-patterned coherence distributions, where crucially, the effective twist angles, layer numbers, and resulting spatiotemporal Moiré patterns can be dynamically tuned through precise frequency control, offering unprecedented flexibility in quantum simulation.

Building on this platform, We develop a 2D Moiré time crystal framework within Floquet phase space that offers a complete understanding of these quantum phenomena, surpassing conventional approaches like period-doubling

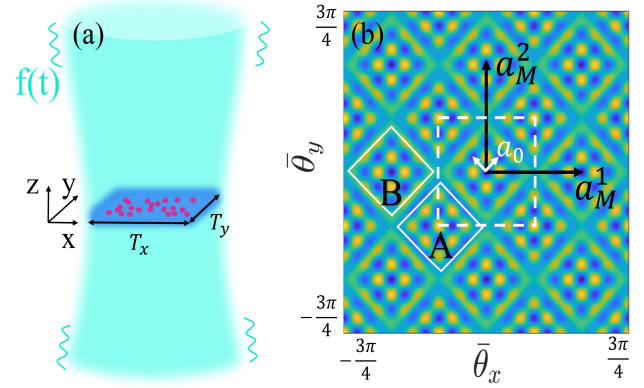


FIG. 1. (a) A schematic diagram of the model depicts ultracold atoms moving within a 2D square potential well (blue) and experiencing perturbation from an additional laser beam (light blue) featuring multi-frequency intensity modulation. (b) 2D FPS effective potential $V_{n=16, m=12}(\bar{\theta}_x, \bar{\theta}_y)$ with depth indicated by color, at twist angle $\alpha \approx 16.26^\circ$ and primary cell periodicity $a_0 = \pi/10$ denoted by the white shorter arrows. Two distinct Moiré patterns, A and B, are observed (bordered by white dashed lines), corresponding to a quadrilateral unit cell with equal-length Moiré vectors $|\mathbf{a}_M^1| = |\mathbf{a}_M^2| = 5a_0$.

oscillation [32] or dynamical localization [33] which only partially capture temporal or spatial behaviors. In this space, where time effectively emulates spatial dimensions to host exotic quantum phases previously confined to spatial systems [34–40], the Moiré lattice enables seamless interconversion between spatial and temporal roles while maintaining essential Moiré characteristics. This approach not only circumvents the need for physical twisted lattices but also uncovers novel spatiotemporal Moiré phases, establishing time as an engineering degree of freedom for advanced twistronics applications.

Model.—We consider a system comprising ultracold atoms confined within a 2D deep potential well, as depicted in Fig. 1(a). Rather than directly constructing additional twisted-bilayer lattice potentials using optical

lattices of different orientations, we introduce small, yet multifrequency perturbations to the atoms in the well. The 2D single-atom Hamiltonian is given by

$$H_{sa} = \frac{p_x^2 + p_y^2}{2m_a} + U(x, y) + V(x, y, t) \quad (1)$$

where p_x and p_y represent the momenta of the atom in the x and y directions, respectively, and m_a is the atom's mass. The terms $U(x, y)$ and $V(x, y, t)$ correspond to the deep 2D trapping and small multi-frequency perturbation potential, respectively. When the frequency of perturbation V matches multiples of an atom's periodic motion frequency in trap U , a lattice structure forms in its Floquet phase space (FPS). Then the periodic dynamics can be modeled using a quasi-energy band approach, akin to recent studies on time crystals [41–43]. By introducing multiple perturbation frequencies and carefully establishing resonant relations, we can create twisted-bilayer lattices or even more intricate lattice structures within FPS.

To be concrete, we approximate U as a 2D infinite square well with width L , so the atomic motion frequencies in the x and y directions are $\Omega_{x,y} = (\pi/L)\sqrt{2E_{x,y}/m_a}$, where $E_{x,y}$ are the initial kinetic energy. We set the perturbation as a 2D quadratic potential, $V = V_0 x^2 y^2 f(t)$, where V_0 is the perturbation strength and $f(t) = \sum_l f_l e^{-i\omega_l t}$ controls the “bobbing” frequency distribution. In action-angle coordinates, the potential expands as

$$V = \sum_{nml} \mathcal{V}_{nml} e^{i(n\theta_x + m\theta_y - \omega_l t)}, \quad (2)$$

with Fourier coefficients $\mathcal{V}_{nml} = \frac{4V_0 L^4 f_l}{\pi^4 n^2 m^2}$, and angle $\theta_x = \text{sign}(p_x)(\pi x/L + \pi/2)$ (similarly for θ_y) [44]. Resonant terms, where $n\theta_x + m\theta_y - \omega_l t = 0$, dominate the perturbation to the atomic dynamics, while other rapidly oscillating terms are negligible (secular approximation).

Considering the angle evolution $\theta_{x,y} \approx \Omega_{x,y}t$, if four perturbation frequencies satisfy the resonant conditions, $\omega_1 = n\Omega_x + m\Omega_y$, $\omega_2 = m\Omega_x + n\Omega_y$, $\omega_3 = n\Omega_x - m\Omega_y$, $\omega_4 = m\Omega_x - n\Omega_y$, where n and m are natural numbers, only four terms survive after the secular approximation. Other terms that are insensitive to approximations, such as accidental resonant terms (where $n'\Omega_x + m'\Omega_y = n\Omega_x + m\Omega_y$) and nearly resonant terms, can be minimized by ensuring that Ω_x and Ω_y are coprime and by keeping the value of $\frac{2V_0 L^2}{\pi^2 m_a \Omega_x \Omega_y}$ sufficiently small.

By further performing a time-dependent canonical coordinate transformation, $\bar{\theta}_{x,y} = \theta_{x,y} - \Omega_{x,y}t$, on H_{sa} , we obtain a static lattice Hamiltonian within the FPS (see supplementary materials for additional details),

$$\begin{aligned} H_{sa} = & \frac{P_{\bar{\theta}_x}^2 + P_{\bar{\theta}_y}^2}{2m_{\text{eff}}} + \mathcal{V}_{nm} [\cos(m\bar{\theta}_x + n\bar{\theta}_y) + \cos(n\bar{\theta}_x - m\bar{\theta}_y) \\ & + \cos(n\bar{\theta}_x + m\bar{\theta}_y) + \cos(m\bar{\theta}_x - n\bar{\theta}_y)], \end{aligned} \quad (3)$$

where $P_{\bar{\theta}_x, \bar{\theta}_y}$ and m_{eff} represent the generalized momenta and effective mass in FPS. The integration of four cosine potential terms, each possessing a uniform depth ($f_l = 1$) but differing in orientation, results in an effective twisted-bilayer square lattice. This structure is characterized by a primary unit cell with a periodicity of $a_0 = 2\pi/\sqrt{n^2 + m^2}$ and a twist angle $\alpha = |\arctan(\frac{m}{2n} - \frac{n}{2m})|$, where (n, m) constitute a Pythagorean triple, ensuring the commensurability condition required for Moiré lattice formation.

Figure 1(b) illustrates the lattice structure, featuring two distinct yet similar square Moiré patterns labeled A and B , where the central region of pattern A forms a barrier while that of pattern B constitutes a deep well. The Moiré unit cell is delineated by the vectors \mathbf{a}_M^1 and \mathbf{a}_M^2 , where the Moiré period is given by $|\mathbf{a}_M^1| = |\mathbf{a}_M^2| = \frac{\bar{a}}{2\sin(\alpha/2)}$ where $\bar{a} = \sqrt{2}a_0$ if $(m+n)/s$ is odd, and $\bar{a} = a_0$ if even, with s being the greatest common divisor of m and n . Remarkably, because the system is not constrained by a physical lattice potential, the geometric structure of the Moiré lattice can be dynamically tuned by altering the frequency distribution of V , which determines the effective lattice orientation, twist angle, and number of layers. This freedom enables the realization of more complex Moiré geometries.

Unlike Moiré lattices in phase space formed by non-commutative x and p [45], our 2D FPS uses commutative coordinates $\bar{\theta}_x$ and $\bar{\theta}_y$, enabling the emergence of all exotic quantum phases similar to those observed in 2D spatial Moiré lattices, especially when atom-atom interaction is considered. Furthermore, the analogous roles of x and t in the coordinate transformation $\theta_x = \text{sign}(p_x)(\frac{\pi x}{L} + \frac{\pi}{2}) - \Omega_x t$ (and similarly for θ_y) highlight the dual manifestation of these FPS Moiré phases. These phases can manifest not only in the spatial domain at a fixed time, even when a spatially twisted lattice potential is absent from the original Hamiltonian, but also in the temporal domain at a fixed position, indicating a unique temporal correlation in dynamics.

Specifically, at a fixed time $t = t_0$, a Moiré lattice potential resembling Fig. 1(b) appears in the (x, y) space, with a primary period $a_0^* = a_0 L/\pi$ and a Moiré period $a_M^* = a_M L/\pi$. Conversely, for a fixed spatial position, despite t being a single variable, distinct dynamical behaviors can be observed across diverse time scales with significant characteristic frequency disparities $\Omega_x \gg \Omega_y$ (In this work, we set $\Omega_x \gg \Omega_y$, the converse is also viable), enabling effective 2D time degrees of freedom. Using two measurement intervals $\Delta t_x \ll \Delta t_y$, time can be represented as

$$t = \Delta t_x j + \Delta t_y k, \quad (4)$$

where j, k are positive integers. Meeting the resonance condition $\Delta t_y \Omega_x = 2\pi$ (i.e., $\Delta t_y = T_x$) ensures θ_x linearly relates to $\Delta t_x j$ and is independent of $\Delta t_y k$ at fixed (x_0, y_0) . Similarly, θ_y linearly relates to $\Delta t_y k$ with a negligible offset $\delta_j = \Omega_y \Delta t_x j$ (because $\Omega_x \gg \Omega_y$), as shown

in the following

$$\bar{\theta}_x = \theta_{x_0} - \Omega_x \Delta t_x j - 2k\pi, \quad (5)$$

$$\bar{\theta}_y = \theta_{y_0} - \Omega_y \Delta t_y k - \delta_j, \quad (6)$$

where the 2D time degrees of freedom are represented by discrete variables (j, k) , but $\Omega_x \Delta t_x, \Omega_y \Delta t_y \ll 2\pi$ ensure sufficient resolution for capturing the Moiré lattice structure in the time domain, with two primary periods $T_0^{x,y} = a_0/\Omega_{x,y}$ and two Moiré periods $T_M^{x,y} = a_M/\Omega_{x,y}$.

Furthermore, based on a similar principle, an even more intriguing spatiotemporal Moiré lattice can arise when we fix just one spatial coordinate and utilize a specific time interval. For example, by fixing $y = y_0$ and $t = \Delta t_y k$, we obtain

$$\bar{\theta}_x = \theta_x - 2\pi k, \quad (7)$$

$$\bar{\theta}_y = \theta_{y_0} - 2\pi \left(\frac{\Omega_y}{\Omega_x} \right) k, \quad (8)$$

which results in an effective two-dimensional spatiotemporal coordinate system (x, k) , from which the spatiotemporal Moiré lattices and Moiré phases emerge. Similarly, an effective (j, y) system can be derived.

To validate our model and reveal the unique Moiré phases across spatial, temporal, and spatiotemporal domains, we numerically simulate the dynamical evolution of ultracold atoms' mean-field wavefunction in the laboratory frame. These simulations utilize the Gross-Pitaevskii (GP) equation,

$$i\hbar \frac{\partial \psi}{\partial t} = (H_{sa}(t) + g\eta N |\psi|^2) \psi, \quad (9)$$

where ψ denotes the condensate wavefunction (initially a wavepacket with given momentum), η is the reduction coefficient arising from the dimensionality reduction of the GP equation from 3D to 2D, N represents the total number of atoms, and g signifies the strength of atom-atom interaction. The nonlinear interaction is crucial for both producing exotic quantum many-body phases and breaking $H_{sa}(t)$'s discrete time translation symmetry, essential for realizing time crystals.

Regional superfluid—Under repulsive interaction, the characteristic atomic quantum phase in the Moiré lattice exhibits behavior as a regional superfluid. It displays Moiré patterns in atomic density, but coherence breaks down between patterns. Within each pattern, coherence is maintained among lattice sites until the boundary, where the potential sharply changes.

The Floquet phase space (FPS) coordinates $(\bar{\theta}_x, \bar{\theta}_y)$ inherently unify spatial and temporal degrees of freedom, allowing selective examination of either specific positions or instants in the laboratory frame to study regional superfluid states. When choosing time points t_0 that are integer multiples of the periods $T_x = 2\pi/\Omega_x$ or

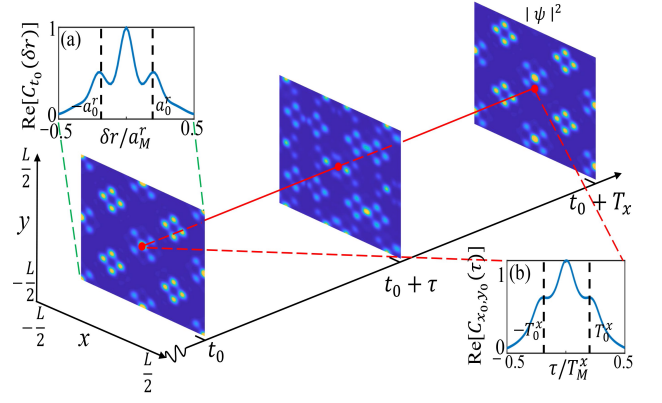


FIG. 2. The atomic probability density $|\psi(x, y, t)|^2$ at three moments is accompanied by insert showing (a) real part of spatial autocorrelation $C_{t_0}(\delta r)$ at $t_0 = 98T_y$ within a spatial Moiré period a_M^r (dashed lines mark spatial primary cell period a_0^r) and (b) real part of temporal autocorrelation $C_{x_0, y_0}(\tau)$ at position (x_0, y_0) (red dot) within a temporal Moiré period $T_M^x = T_x/4$ (dashed lines mark temporal primary cell period $T_0^x = T_x/20$), using parameters $\Omega_x = \pi \times 10^3 E_r/\hbar$, $\Omega_x/\Omega_y = 64\pi$, $\mathcal{V}_{16,12} = 0.35 E_r$, $E_r = \frac{2\hbar^2 \pi^2}{m_a L a_0}$, and $\eta g N = 10^2 \hbar^2/m_a$.

$T_y = 2\pi/\Omega_y$, the atomic density and coherence distributions in laboratory coordinates (x, y, t_0) precisely correspond to those in FPS, aside from minor displacements from the linear coordinate transformation. At these moments, the system exhibits clear regional superfluidity with Moiré-patterned density distributions in physical space (as the three slices shown in Fig. 2), despite the absence of any physical Moiré lattice potential. This phenomenon emerges because only the driving-frequency-resonant Fourier components of the perturbation potential significantly influence the dynamics, effectively creating a virtual Moiré lattice structure in the laboratory frame.

The spatial regional superfluid state can be confirmed using the spatial autocorrelation function to measure atom phase correlation length,

$$C_{t_0}(\delta \mathbf{r}) = \int \psi^*(\mathbf{r}, t_0) \psi(\mathbf{r} + \delta \mathbf{r}, t_0) d^2 \mathbf{r} \quad (10)$$

with time t_0 fixed and $\delta \mathbf{r}$ denoting 2D spatial separation distance vector. For simplicity, we consider the separation along the direction where $\delta y = \delta x$, and the results are presented in insert (a) of Fig. 2. In this state, the spatial long-range coherence characteristic of conventional superfluids is absent. Instead, coherence is confined to short ranges and is most pronounced within a primary spatial period $a_0^r = L/10$. However, this coherence diminishes rapidly when the separation δr exceeds the spatial Moiré period $a_M^r = L/2$, which aligns with the Moiré lattice structure observed in FPS before applying the coordinate transformation.

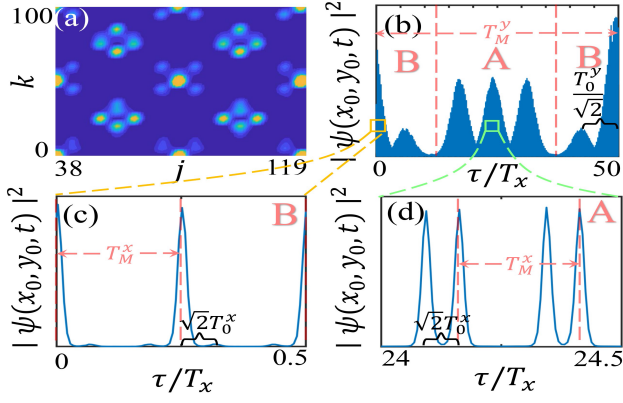


FIG. 3. (a) $|\psi(x_0, y_0, t)|^2$ in (j, k) temporal coordinates ($t = \Delta t_x j + \Delta t_y k + 98T_y$) shows temporal Moiré superfluidity. (b) Evolution versus $\tau = t - 98T_y$ reveals Moiré patterns A/B at T_y scale. (c,d) Higher-resolution views show nested Moiré structures at T_x scale. Parameters as in Fig. 2.

By contrast, to confirm the regional superfluid state in the time domain, we used the temporal autocorrelation function for a fixed spatial position (x_0, y_0) ,

$$C_{x_0, y_0}(\tau) = \int \psi^*(x_0, y_0, t) \psi(x_0, y_0, t + \tau) dt. \quad (11)$$

As depicted in insert (b) of Fig. 2, the temporal coherence is prominent within a primary period T_0^x , and diminishes to zero when the separation τ surpasses a temporal Moiré period of T_M^x , mirroring the behavior observed in the spatial domain. The other temporal Moiré structure with periods T_0^y and T_M^y is absent here due to the longer time scales it requires.

To illustrate the overall structure and dynamics of this temporal, regional superfluid state, Fig. 3(b) depicts the evolution of the probability density $|\psi(t)|^2$ at (x_0, y_0) over a duration of $50T_x$, using a continuous physical time coordinate. Panels (c) and (d) provide locally enlarged views of this evolution. Alternatively, Fig. 3(a) employs two discrete time coordinates (j, k) derived from the transformations outlined in Eqs. (4), (5), and (6), revealing a 2D Moiré structure with dual patterns (A and B) that precisely correspond to the spatial density distribution in Fig. 2. Given the significant disparity between the time intervals Δt_x and Δt_y in transformation Eq. (4), variations in $|\psi(t)|^2$ along the j coordinate reflect dynamics occurring within the T_x time scale, whereas changes along the k coordinate correspond to dynamics within the T_y time scale. Consequently, Moiré patterns A and B exhibit similar probability variations in the j and k coordinates, respectively, yet the corresponding periodic dynamics are observable in two distinct time scales. In Fig. 3(b), fine vibrations are indistinguishable, but the envelope vibrations exhibit two periodic dynamics, a small period $T_0^y/\sqrt{2}$, and a large period T_M^y . These correspond to the alternating Moiré patterns ob-

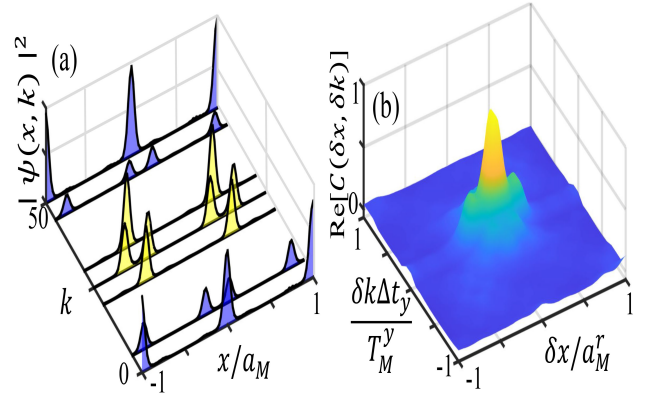


FIG. 4. (a) Slices of probability density in the coordinate (x, k) reveals a 2D spatiotemporal Moiré lattice, and the two Moiré patterns are denoted with different shading colors. (b) Spatiotemporal autocorrelation $C(\delta x, \delta k)$ in the 2D coordinate (x, k) possesses a spatiotemporal coherent length up Moiré scale. Parameters as in Fig. 2.

served as the time coordinates in Fig. 3(a) advance along the slash line defined by Eq. (4). In the enlarged views (c) and (d), two distinct biperiodic vibration dynamics are observable, both characterized by a large period T_M^x and a small period $\sqrt{2}T_0^x$, yet they exhibit different timing sequences. These correspond to various Moiré patterns in coordinate j for differing values of k . A critical observation is that, for irrational Ω_x/Ω_y , the evolution exhibits quasi-periodicity instead of exact periodicity. While $|\psi(t)|^2$ shares quasi-periodicity with $H_{sa}(t)$, the quasi-periods of $\psi(t)$ differ by a $|n - m|$ -fold factor derived from $\sqrt{2(m^2 + n^2)} \sin \frac{\alpha}{2}$. This fold relationship, arising from wavefunction phase variations across Moiré superfluid regions, directly evidences discrete time translation symmetry breaking—a hallmark of time crystal behavior.

In addition to unveiling the 2D regional superfluid state in both spatial and temporal coordinates, our scheme also permits the emergence of a spatiotemporal regional superfluid state. This state is distinguished by a probability density distribution exhibiting a Moiré pattern in the (x, k) coordinates and by the presence of atomic phase coherence across both spatial and temporal Moiré periods. As illustrated in Fig. 4(a), for a constant time k , only one type of periodic density distribution is evident along the x coordinate. As time k varies, two distinct types of periodic density distributions alternately appear, corresponding to Moiré patterns A and B. An analogous alternation is observed in the temporal periodic density distribution as the position x changes. A spatiotemporal correlation $C(\delta x, \delta k)$ defined through the combination of Eqs. (10) and (11) is depicted in Fig. 4(b). The bulge observed in the center emphasizes that coherence can persist within a range corresponding to the spatiotemporal Moiré period $a_M = \sqrt{\delta \tau^2 + \delta x^2}$, indicating

a necessary trade-off between temporal delay and spatial distance when leveraging this quantum coherence.

Conclusion—We demonstrate how ultracold atoms in a 2D deep potential well, subjected to multifrequency perturbations but requiring neither spatial periodicity nor multilayer potentials, can emulate twistorics physics. Their quantum dynamics form a 2D Moiré time crystal when prepared with proper initial velocities and interatomic interaction strength, exhibiting regional superfluidity characterized by Moiré-patterned probability distributions and coherence lengths across spatial, temporal, or spatiotemporal domains. For cold ^{39}K atoms in a $\sim 100\mu\text{m}$ box potential with initial velocities $v_x \sim 10\text{m/s}$ and $v_y \sim 0.1\text{m/s}$, we obtain a $\sim 10\mu\text{m}$ spatial Moiré pattern and two distinct temporal Moiré periods $T_M^x \sim 1\mu\text{s}$ and $T_M^y \sim 0.1\text{ms}$ [46], which are $|2mn/(m^2 - n^2)|$ times the primary periods. Increasing the perturbation frequency multiples n and m while keeping them close could enhance Moiré-primary period separation, generating carrier-envelope structure analogous to mode-locked laser [47], and paving the way for ultrafast atom lasers [48]. The scheme accommodates other Moiré phases through interaction and perturbation frequency tuning, extends naturally to 3D Moiré crystals [49], and suggests possible space-time crystal realizations [50–52].

Acknowledgements—This work was supported by the Innovation Program for Quantum Science and Technology (No. 2021ZD0303200); the National Science Foundation of China (No. 12374328, No. 11974116, and No. 12234014); the Shanghai Science and Technology Innovation Project (No. 24LZ1400600); the Shanghai Science and Technology Major Project (No. 2019SHZDZX01); the National Key Research and Development Program of China (No. 2016YFA0302001); the Fundamental Research Funds for the Central Universities; the Chinese National Youth Talent Support Program, and the Shanghai Talent program.

* wpz@sjtu.edu.cn

† ky Zhang@phy.ecnu.edu.cn

- [1] Y. Cao, V. Fatemi, S. Fang, K. Watanabe, T. Taniguchi, E. Kaxiras, and P. Jarillo-Herrero, Unconventional superconductivity in magic-angle graphene superlattices, *Nature* **556**, 43 (2018).
- [2] M. Yankowitz, S. Chen, H. Polshyn, Y. Zhang, K. Watanabe, T. Taniguchi, D. Graf, A. F. Young, and C. R. Dean, Tuning superconductivity in twisted bilayer graphene, *Science* **363**, 1059 (2019).
- [3] A. Kerelsky, L. J. McGilly, D. M. Kennes, L. Xian, M. Yankowitz, S. Chen, K. Watanabe, T. Taniguchi, J. Hone, C. Dean, *et al.*, Maximized electron interactions at the magic angle in twisted bilayer graphene, *Nature* **572**, 95 (2019).
- [4] X. Lu, P. Stepanov, W. Yang, M. Xie, M. A. Aamir, I. Das, C. Urgell, K. Watanabe, T. Taniguchi, G. Zhang, *et al.*, Superconductors, orbital magnets and correlated states in magic-angle bilayer graphene, *Nature* **574**, 653 (2019).
- [5] Y. Choi, J. Kemmer, Y. Peng, A. Thomson, H. Arora, R. Polski, Y. Zhang, H. Ren, J. Alicea, G. Refael, *et al.*, Electronic correlations in twisted bilayer graphene near the magic angle, *Nature Physics* **15**, 1174 (2019).
- [6] X. Liu, Z. Wang, K. Watanabe, T. Taniguchi, O. Vafek, and J. Li, Tuning electron correlation in magic-angle twisted bilayer graphene using coulomb screening, *Science* **371**, 1261 (2021).
- [7] E. M. Spanton, A. A. Zibrov, H. Zhou, T. Taniguchi, K. Watanabe, M. P. Zaletel, and A. F. Young, Observation of fractional chern insulators in a van der waals heterostructure, *Science* **360**, 62 (2018).
- [8] Y. Xie, A. T. Pierce, J. M. Park, D. E. Parker, E. Khalaf, P. Ledwith, Y. Cao, S. H. Lee, S. Chen, P. R. Forrester, *et al.*, Fractional chern insulators in magic-angle twisted bilayer graphene, *Nature* **600**, 439 (2021).
- [9] S. Kezilebieke, V. Vano, M. N. Huda, M. Aapro, S. C. Ganguli, P. Liljeroth, and J. L. Lado, Moiré-enabled topological superconductivity, *Nano Letters* **22**, 328 (2022).
- [10] J. Cai, E. Anderson, C. Wang, X. Zhang, X. Liu, W. Holtzmann, Y. Zhang, F. Fan, T. Taniguchi, K. Watanabe, *et al.*, Signatures of fractional quantum anomalous hall states in twisted mote2, *Nature* **622**, 63 (2023).
- [11] Q. Tong, H. Yu, Q. Zhu, Y. Wang, X. Xu, and W. Yao, Topological mosaics in moiré superlattices of van der waals heterobilayers, *Nature Physics* **13**, 356 (2017).
- [12] Y. Cao, V. Fatemi, A. Demir, S. Fang, S. L. Tomarken, J. Y. Luo, J. D. Sanchez-Yamagishi, K. Watanabe, T. Taniguchi, E. Kaxiras, *et al.*, Correlated insulator behaviour at half-filling in magic-angle graphene superlattices, *Nature* **556**, 80 (2018).
- [13] A. L. Sharpe, E. J. Fox, A. W. Barnard, J. Finney, K. Watanabe, T. Taniguchi, M. Kastner, and D. Goldhaber-Gordon, Emergent ferromagnetism near three-quarters filling in twisted bilayer graphene, *Science* **365**, 605 (2019).
- [14] E. Codecido, Q. Wang, R. Koester, S. Che, H. Tian, R. Lv, S. Tran, K. Watanabe, T. Taniguchi, F. Zhang, *et al.*, Correlated insulating and superconducting states in twisted bilayer graphene below the magic angle, *Science Advances* **5**, eaaw9770 (2019).
- [15] G. Chen, L. Jiang, S. Wu, B. Lyu, H. Li, B. L. Chittari, K. Watanabe, T. Taniguchi, Z. Shi, J. Jung, *et al.*, Evidence of a gate-tunable mott insulator in a trilayer graphene moiré superlattice, *Nature Physics* **15**, 237 (2019).
- [16] K. Tran, G. Moody, F. Wu, X. Lu, J. Choi, K. Kim, A. Rai, D. A. Sanchez, J. Quan, A. Singh, *et al.*, Evidence for moiré excitons in van der waals heterostructures, *Nature* **567**, 71 (2019).
- [17] Z. Zheng, Q. Ma, Z. Bi, S. de La Barrera, M.-H. Liu, N. Mao, Y. Zhang, N. Kiper, K. Watanabe, T. Taniguchi, *et al.*, Unconventional ferroelectricity in moiré heterostructures, *Nature* **588**, 71 (2020).
- [18] Z. Meng, L. Wang, W. Han, F. Liu, K. Wen, C. Gao, P. Wang, C. Chin, and J. Zhang, Atomic bose-einstein condensate in twisted-bilayer optical lattices, *Nature* **615**, 231 (2023).

- [19] P. Wang, Y. Zheng, X. Chen, C. Huang, Y. V. Kartashov, L. Torner, V. V. Konotop, and F. Ye, Localization and delocalization of light in photonic moiré lattices, *Nature* **577**, 42 (2020).
- [20] Q. Fu, P. Wang, C. Huang, Y. V. Kartashov, L. Torner, V. V. Konotop, and F. Ye, Optical soliton formation controlled by angle twisting in photonic moiré lattices, *Nature Photonics* **14**, 663 (2020).
- [21] B. Lou, B. Wang, J. A. Rodríguez, M. Cappelli, and S. Fan, Tunable guided resonance in twisted bilayer photonic crystal, *Science Advances* **8**, eadd4339 (2022).
- [22] H.-Y. Luan, Y.-H. Ouyang, Z.-W. Zhao, W.-Z. Mao, and R.-M. Ma, Reconfigurable moiré nanolaser arrays with phase synchronization, *Nature* **624**, 282 (2023).
- [23] D. Yu, G. Li, L. Wang, D. Leykam, L. Yuan, and X. Chen, Moiré lattice in one-dimensional synthetic frequency dimension, *Physical Review Letters* **130**, 143801 (2023).
- [24] V. Montenegro, M. G. Genoni, A. Bayat, and M. G. Paris, Quantum metrology with boundary time crystals, *Communications Physics* **6**, 304 (2023).
- [25] A. Cabot, F. Carollo, and I. Lesanovsky, Continuous sensing and parameter estimation with the boundary time crystal, *Physical Review Letters* **132**, 050801 (2024).
- [26] F. Iemini, R. Fazio, and A. Sanpera, Floquet time crystals as quantum sensors of ac fields, *Physical Review A* **109**, L050203 (2024).
- [27] R. Yousefjani, K. Sacha, and A. Bayat, Discrete time crystal phase as a resource for quantum-enhanced sensing, *Physical Review B* **111**, 125159 (2025).
- [28] D. Gribben, A. Sanpera, R. Fazio, J. Marino, and F. Iemini, Boundary time crystals as ac sensors: Enhancements and constraints, *SciPost Physics* **18**, 100 (2025).
- [29] P. T. Dumitrescu, J. G. Bohnet, J. P. Gaebler, A. Hankin, D. Hayes, A. Kumar, B. Neyenhuis, R. Vasseur, and A. C. Potter, Dynamical topological phase realized in a trapped-ion quantum simulator, *Nature* **607**, 463 (2022).
- [30] A. González-Tudela and J. I. Cirac, Cold atoms in twisted-bilayer optical potentials, *Physical Review A* **100**, 053604 (2019).
- [31] T. Salamon, A. Celi, R. W. Chhajlany, I. Frérot, M. Lewenstein, L. Tarruell, and D. Rakshit, Simulating twistrionics without a twist, *Physical Review Letters* **125**, 030504 (2020).
- [32] P. S. Lindsay, Period doubling and chaotic behavior in a driven anharmonic oscillator, *Physical Review Letters* **47**, 1349 (1981).
- [33] A. Eckardt, M. Holthaus, H. Lignier, A. Zenesini, D. Ciampini, O. Morsch, and E. Arimondo, Exploring dynamic localization with a bose-einstein condensate, *Physical Review A* **79**, 013611 (2009).
- [34] K. Sacha, Anderson localization and mott insulator phase in the time domain, *Scientific reports* **5**, 10787 (2015).
- [35] S. Autti, V. Eltsov, and G. Volovik, Observation of a time quasicrystal and its transition to a superfluid time crystal, *Physical Review Letters* **120**, 215301 (2018).
- [36] K. Giergiel, A. Miroszewski, and K. Sacha, Time crystal platform: From quasicrystal structures in time to systems with exotic interactions, *Physical Review Letters* **120**, 140401 (2018).
- [37] K. Giergiel, A. Dauphin, M. Lewenstein, J. Zakrzewski, and K. Sacha, Topological time crystals, *New Journal of Physics* **21**, 052003 (2019).
- [38] A. E. Kopaei, X. Tian, K. Giergiel, and K. Sacha, Topological molecules and topological localization of a rydberg electron on a classical orbit, *Physical Review A* **106**, L031301 (2022).
- [39] L. Guo, V. Peano, and F. Marquardt, Phase space crystal vibrations: Chiral edge states with preserved time-reversal symmetry, *Physical Review B* **105**, 094301 (2022).
- [40] A. E. Kopaei, K. Giergiel, and K. Sacha, Topologically protected quantized changes of the distance between atoms, *Physical Review Research* **6**, 043173 (2024).
- [41] L. Guo, M. Marthaler, and G. Schön, Phase space crystals: a new way to create a quasienergy band structure, *Physical Review Letters* **111**, 205303 (2013).
- [42] K. Sacha, Modeling spontaneous breaking of time-translation symmetry, *Physical Review A* **91**, 033617 (2015).
- [43] P. Matus and K. Sacha, Fractional time crystals, *Physical Review A* **99**, 033626 (2019).
- [44] K. Zhang, W. Liang, P. Meystre, and W. Zhang, Quantum metrology with bloch oscillations in floquet phase space, *Physical Review A* **107**, 022605 (2023).
- [45] L. Guo and V. Peano, Engineering arbitrary hamiltonians in phase space, *Physical Review Letters* **132**, 023602 (2024).
- [46] T. Klostermann, C. R. Cabrera, H. von Raven, J. F. Wienand, C. Schweizer, I. Bloch, and M. Aidelsburger, Fast long-distance transport of cold cesium atoms, *Physical Review A* **105**, 043319 (2022).
- [47] D. J. Jones, S. A. Diddams, J. K. Ranka, A. Stentz, R. S. Windeler, J. L. Hall, and S. T. Cundiff, Carrier-envelope phase control of femtosecond mode-locked lasers and direct optical frequency synthesis, *Science* **288**, 635 (2000).
- [48] N. Robins, P. Altin, J. Debs, and J. Close, Atom lasers: Production, properties and prospects for precision inertial measurement, *Physics Reports* **529**, 265 (2013).
- [49] C. Wang, C. Gao, J. Zhang, H. Zhai, and Z.-Y. Shi, Three-dimensional moiré crystal in ultracold atomic gases, *Physical Review Letters* **133**, 163401 (2024).
- [50] S. Xu and C. Wu, Space-time crystal and space-time group, *Physical Review Letters* **120**, 096401 (2018).
- [51] G. Żlabys, C.-h. Fan, E. Anisimovas, and K. Sacha, Six-dimensional time-space crystalline structures, *Physical Review B* **103**, L100301 (2021).
- [52] Y. Peng, Topological space-time crystal, *Physical Review Letters* **128**, 186802 (2022).
- [53] D. Delande, L. Morales-Molina, and K. Sacha, Three-dimensional localized-delocalized anderson transition in the time domain, *Physical Review Letters* **119**, 230404 (2017).

Supplemental Materials

2D ACTION-ANGLE TRANSFORM AND SECULAR APPROXIMATION

In the single-atom case, the atom is confined by a conservative two-dimensional potential and perturbed by a time-dependent potential. The Hamiltonian describing this system is given by

$$H_{sa} = \frac{p_x^2 + p_y^2}{2m_a} + U(x, y) + V(x, y, t) \quad (S1)$$

where $U(x, y)$ represents an infinite square well defined as

$$U(x, y) = \begin{cases} 0 & \text{if } |x|, |y| < \frac{L}{2}, \\ \infty & \text{otherwise} \end{cases} \quad (S2)$$

The time-dependent perturbation is given in the form

$$V(x, y, t) = V_0 x^2 y^2 f(t), \quad (S3)$$

where the function $f(t)$ describing the temporal variation is

$$f(t) = \cos(\omega_1 t) + \cos(\omega_2 t) + \cos(\omega_3 t) + \cos(\omega_4 t). \quad (S4)$$

Without the influence of perturbation, the atom's motion can be decomposed into components along the x and y dimensions, with the periods determined by the initial kinetic energies E_x and E_y , respectively. This periodic motion can be transformed from the (x, y) coordinate space into a 2D angular space (θ_x, θ_y) using the action-angle transformation,

$$I_x = \frac{L\sqrt{2m_a E_x}}{\pi}, \quad (S5)$$

$$\theta_x = \frac{\pi}{L} \left(x + \frac{L}{2} \right) \text{sign}(p_x), \quad (S6)$$

with analogous expressions for I_y and θ_y in terms of E_y and y . The evolution of the angles is constrained within the range $(-\pi, \pi]$ and is governed by the frequencies

$$\Omega_{x,y} = \dot{\theta}_{x,y} = \frac{\partial E_{x,y}}{\partial I_{x,y}} = \frac{\pi}{L} \sqrt{\frac{2E_{x,y}}{m_a}} \quad (S7)$$

In angular space, the first two terms of H_{sa} becomes

$$H_0(I_x, I_y) = \frac{\pi^2(I_x^2 + I_y^2)}{2m_a L^2}, \quad (S8)$$

and the perturbation becomes

$$V(x, y, t) = \frac{V_0 L^4}{\pi^4} \left(|\theta_x| - \frac{\pi}{2} \right)^2 \left(|\theta_y| - \frac{\pi}{2} \right)^2 f(t) = \sum_{m,n,l} \mathcal{V}_{nml} e^{i(n\theta_x + m\theta_y - \omega_l t)}, \quad (S9)$$

with Fourier coefficients

$$\mathcal{V}_{nml} = \frac{4V_0 L^4 f_l}{\pi^4 n^2 m^2}, \quad (S10)$$

where n, m are even numbers, yielding the Hamiltonian

$$H_{sa} = H_0(I_x, I_y) + V(\theta_x, \theta_y, t). \quad (S11)$$

Without perturbations, $\theta_{x,y} \sim \Omega_{x,y}t$, enabling use of secular approximation to keep only four resonant terms in V satisfying:

$$\omega_1 = n\Omega_x + m\Omega_y, \quad (\text{S12})$$

$$\omega_2 = m\Omega_x + n\Omega_y, \quad (\text{S13})$$

$$\omega_3 = n\Omega_x - m\Omega_y, \quad (\text{S14})$$

$$\omega_4 = m\Omega_x - n\Omega_y, \quad (\text{S15})$$

while rapidly oscillating nonresonant terms are discarded. In Floquet phase space (defined by slow variables $\bar{\theta}_{x,y} = \theta_{x,y} - \Omega_{x,y}t$), V becomes a twisted square lattice potential:

$$\mathcal{V}(\bar{\theta}_x, \bar{\theta}_y) = \frac{4V_0L^4}{\pi^4n^2m^2} [\cos(n\bar{\theta}_x + m\bar{\theta}_y) + \cos(m\bar{\theta}_x + n\bar{\theta}_y) + \cos(n\bar{\theta}_x - m\bar{\theta}_y) + \cos(m\bar{\theta}_x - n\bar{\theta}_y)]. \quad (\text{S16})$$

However, in systems with two degrees of freedom (θ_x, θ_y) , accidental resonances may emerge when distinct mode combinations satisfy $n\Omega_x + m\Omega_y = n'\Omega_x + m'\Omega_y$ for different integer pairs $(n, m) \neq (n', m')$. We adopt an irrational ratio for Ω_x/Ω_y to suppress such spurious resonances.

Even with irrational ratios, near-resonant terms persist where $|n\Omega_x + m\Omega_y - \omega_l|$ becomes small. These higher-order perturbations can accumulate, breaking the secular approximation. To address this issue, we utilize a time-dependent canonical transformation to separate resonant and nonresonant terms, thereby identifying the conditions that minimize the contribution of near-resonant terms. The generating function for this transformation, structured according to the perturbation strength V_0 , is expressed as

$$G = G^{(0)} + G^{(1)}, \quad (\text{S17})$$

where the zeroth-order term is given by

$$G^{(0)} = I'_x(\theta_x - \Omega_x t) + I'_y(\theta_y - \Omega_y t), \quad (\text{S18})$$

and the first-order term is

$$G^{(1)} = i \sum'_{n,m,l} \left[\frac{\mathcal{V}_{nml}}{n\Omega_x + m\Omega_y + \omega_l} e^{i(n\theta_x + m\theta_y + \omega_l t)} - \frac{\mathcal{V}_{nml}}{n\Omega_x + m\Omega_y - \omega_l} e^{-i(n\theta_x + m\theta_y - \omega_l t)} \right], \quad (\text{S19})$$

where the prime on the summation symbol indicates that resonant terms are omitted. The transformed Hamiltonian H_{sa} becomes

$$H'_{sa} = H_0 \left(I'_x + \partial_{\theta_x} G^{(1)}, I'_y + \partial_{\theta_y} G^{(1)} \right) + V(\bar{\theta}_x, \bar{\theta}_y, t) + \partial_t G. \quad (\text{S20})$$

We expand H'_{sa} to second order in the action deviations $P_{\bar{\theta}_x, \bar{\theta}_y} \equiv I'_{x,y} - I_{x,y}$, which serve as conjugate momenta in the Floquet phase space. After removing the trivial terms, we obtain the effective Hamiltonian

$$\mathcal{H}_{sa} = \frac{P_{\bar{\theta}_x}^2 + P_{\bar{\theta}_y}^2}{2m_{\text{eff}}} + \mathcal{V}(\bar{\theta}_x, \bar{\theta}_y) + O(V_0^2), \quad (\text{S21})$$

where $m_{\text{eff}} = m_a L^2 / \pi^2$ is the effective mass. The second-order potential contains all nonresonant contributions,

$$O(V_0^2) = \frac{\pi^2}{2m_a L^2} [(\partial_{\theta_x} G^{(1)})^2 + (\partial_{\theta_y} G^{(1)})^2] = \frac{\pi^2}{2m_a L^2} \sum'_{\substack{n,m,l \\ n',m',l'}} \frac{\mathcal{V}_{nml} \mathcal{V}_{n'm'l'} (nn' + mm') e^{i[(n+n')\bar{\theta}_x + (m+m')\bar{\theta}_y + \Delta t]}}{(n\Omega_x + m\Omega_y + \omega_l)(n'\Omega_x + m'\Omega_y - \omega_{l'})} + \dots, \quad (\text{S22})$$

with oscillating frequency $\Delta \equiv (\omega_l - \omega_{l'}) + (n + n')\Omega_x + (m + m')\Omega_y$ (we show one representative term, with others following similarly). Large detunings allow neglecting $O(V_0^2)$ due to rapid oscillations, recovering the main-text Hamiltonian. Near-resonant cases, however, amplify $O(V_0^2)$ through small denominators. To ensure that $O(V_0^2)$ is still much smaller than $\mathcal{V}(\bar{\theta}_x, \bar{\theta}_y)$, it leads to the condition

$$\frac{2L^2}{\pi^2 m_a} \frac{V_0}{\Omega_x \Omega_y} \frac{\mathcal{F}_{nml} \mathcal{F}_{n'm'l'}}{\mathcal{F}_{n_0 m_0 l}} (nn' + mm') \ll \delta \delta', \quad (\text{S23})$$

where $\delta \equiv |n + m \frac{\Omega_y}{\Omega_x} \pm \frac{\omega_l}{\Omega_x}|$ and $\delta' \equiv |n' \frac{\Omega_x}{\Omega_y} + m' \pm \frac{\omega_{l'}}{\Omega_y}|$ are normalized detunings, with $\mathcal{F}_{nml} = \mathcal{V}_{nml}/V_0 L^4$ denoting normalized Fourier coefficients of the perturbation potential ($\mathcal{F}_{n_0 m_0 l}$ are the resonant terms). To suppress the left side, except for keeping $2V_0 L^2 / \pi^2 m_a \Omega_x \Omega_y$ small we can employ perturbation potentials with rapidly decaying \mathcal{F}_{nml} .